

Cover Page



Universiteit Leiden



The handle <http://hdl.handle.net/1887/138639> holds various files of this Leiden University dissertation.

Author: Mandal, S.

Title: Revealing the nature of new low-frequency radio source populations

Issue Date: 2020-12-10

Chapter 5

Extremely deep 150 MHz source counts from the LoTSS Deep Fields

Based on
S. Mandal, I. Prandoni, M. J. Hardcastle, T. W. Shimwell, H. T. Intema,
C. Tasse, R. J. van Weeren, H. Algera, K. L. Emig, H. J. A. Röttgering,
D. J. Schwarz, T. M. Siewert, P. N. Best, M. Bonato, M. Bondi, M. J. Jarvis,
R. Kondapally, S. K. Leslie, V. H. Mahatma, J. Sabater,
E. Retana-Montenegro, W. L. Williams et al. Submitted to A&A

5.1 Introduction

Large-area radio surveys are very important for statistical studies of radio source populations, addressing astrophysical properties and cosmological evolution of radio galaxies, quasars and starburst galaxies. In the past, several wide-area radio surveys were carried out at low radio frequencies, such as the Cambridge Surveys (3C, 4C, 6C, and 7C at around 160 MHz: [Edge et al. 1959](#), [Bennett 1962](#), [Pilkington & Scott 1965](#), [Gower et al. 1967](#), [Baldwin et al. 1985](#)). However, calibration of low-frequency radio data is challenging due to the direction-dependent, time-varying effects of the ionosphere that affects both the amplitude and the phase of the radio signal. Since these effects are only prominent in the MHz regime, the focus of wide-area/all-sky radio surveys switched to around 1 GHz in the last decades, resulting in the NRAO VLA Sky Survey (NVSS: [Condon et al. 1998](#)), the Sydney University Molonglo Sky Survey (SUMSS: [Mauch et al. 2003](#)) and the Faint Images of the Radio Sky at Twenty-Centimeters (FIRST) survey ([Becker et al. 1995](#); [White et al. 1997](#)).

The higher sensitivity and higher spatial resolution of surveys at GHz frequencies also allowed us to probe deeper and deeper flux densities, and today we have several deep surveys covering degree-scale fields, and sensitive to the sub-mJy and μ Jy radio populations (see e.g. [Prandoni et al. 2000a,b, 2006](#); [Hopkins et al. 2003](#); [Schinnerer et al. 2004, 2007](#); [Hales et al. 2014b](#); [Smolčić et al. 2017](#); [Prandoni et al. 2018](#)). After many years of studies, it is now well established that the sub-mJy radio population has a composite nature. Radio-loud (RL) active galactic nuclei (AGNs) are dominant down to 1.4 GHz flux densities of 200-300 μ Jy and star-forming galaxies (SFGs) become dominant below about 100-200 μ Jy ([Smolčić et al. 2008](#); [Bonzini et al. 2013](#); [Prandoni et al. 2018](#); [Bonato et al. 2020](#)). A significant fraction of the sources below 100 μ Jy can also show signatures of AGN activity in the host galaxy at other bands (IR, optical, X-ray), but rarely display the large-scale radio jets and lobes typical of classical radio galaxies. Most of them are unresolved or barely resolved on a few arcsec scale, i.e. on scales similar to the host galaxy size. The origin of the radio emission in these (so-called radio-quiet) AGN is debated: it may come from star formation in the host galaxy ([Padovani et al. 2011, 2015](#), [Bonzini et al. 2013, 2015](#); [Ocran et al. 2017](#); [Bonato et al. 2017](#)) or from low-level nuclear activity ([White et al. 2015, 2017](#); [Maimi et al. 2016](#); [Herrera Ruiz et al. 2016, 2017](#); [Hartley et al. 2019](#)). Most likely, such AGN are composite systems where star formation and AGN-triggered radio emission co-exist over a wide range of relative contributions (e.g. [Delvecchio et al. 2017](#)). This scenario is also supported

by the modeling work of [Mancuso et al. \(2017\)](#), see also [Macfarlane et al. in prep.](#)).

Being sensitive to SFGs up to the epoch of the peak of their activity ($z \sim 2 - 3$), and reaching for the first time the dominant radio-quiet (RQ) AGN population, deep radio surveys probing the μJy regime can be used as a very important dust/gas-obscuration-free tool to study both AGN activity and star formation and how they evolve with cosmic time. However, to overcome uncertainties introduced by low statistics, cosmic variance effects ([Heywood et al. 2013](#)) and other systematics ([Condon et al. 2012](#)), deep-radio surveys that cover wide areas ($\gg 1 \text{ deg}^2$) and have multi-band ancillary data are needed. Such wide-area surveys are also useful to investigate the role of environment in driving the growth of galaxies and SMBH, and to better trace rare radio source populations.

With the advent of a new generation of low-frequency telescopes and better data processing techniques we can now revisit the radio sky at low-frequency. With the Murchison Widefield Array (MWA; [Lonsdale et al. 2009](#)), [Wayth et al. \(2015\)](#) have carried out the GaLactic and Extragalactic All-sky MWA survey (GLEAM; [Hurley-Walker et al. 2017](#)), reaching a sensitivity of a few mJy beam^{-1} at a resolution of a few arcminutes. The GMRT has significantly improved the low-frequency view of the radio sky in terms of sensitivity and angular resolution. This has already been shown in a few low-frequency surveys centred around 150 MHz (e.g.: [Ishwara-Chandra et al. 2010](#), [Sirothia et al. 2009](#), [Intema et al. 2011](#), [Intema et al. 2017](#)).

The Low Frequency Array (LOFAR; [van Haarlem et al. 2013](#)) is one of the key pathfinders to the Square Kilometre Array (SKA). Most of the LOFAR antennas are based in the Netherlands, with baseline lengths ranging from 100 meters to 120 km. Additional remote stations are located throughout various countries in Europe. The longest baseline of LOFAR can provide a resolution of $0.3''$ at 150 MHz. The combination of LOFAR's large field of view, wide range of baseline lengths, and large fractional bandwidth makes it a powerful instrument for performing large area and deep sky surveys. The LOFAR Two Meter Sky Survey (LoTSS) is an ongoing project in which the whole northern sky is observed with a sensitivity better than $100\mu\text{Jy beam}^{-1}$ at the resolution of $6''$ allowed by the Dutch LOFAR stations. The first data release (DR1) is described by [Shimwell et al. \(2017\)](#) and [Shimwell et al. \(2019\)](#). The LoTSS also includes deeper observations of a number of pre-selected regions, where the aim is to eventually reach an rms depth of $10 \mu\text{Jy beam}^{-1}$ at 150 MHz ([Röttgering et al. 2011](#)). In order to scientifically exploit these more sensitive surveys (collectively known as LoTSS Deep Fields), complementary multi-wavelength data

are necessary, most notably to identify the host galaxies of the extra-galactic radio sources and determine their redshift. For this reason observations were focused on fields with the highest quality multi-wavelength data available. The Lockman Hole, the Boötes and the European Large-Area ISO Survey-North 1 (ELAIS-N1) fields are the deepest of the LoTSS Deep Fields so far (see Tasse et al 2020; Sabater et al. 2020; respectively paper I and II of this series). All have rich multi-wavelength ancillary data, covering a broad range of the electromagnetic spectrum, from X-ray to radio bands.

The Lockman Hole (LH hereafter) is one of the best studied extragalactic regions of the sky. It is characterized by a very low column density of Galactic HI (Lockman et al. 1986) making it an ideal field to study extragalactic sources with deep observations in the mid-IR/FIR/sub-mm (Lonsdale et al. 2003; Mauduit et al. 2012, Oliver et al. 2012), optical/NIR (Muzzin et al. 2009; Fotopoulou et al. 2012; Hildebrandt et al. 2016), and X-ray (Polletta et al. 2006, Brunner et al. 2008). A variety of radio surveys cover limited areas within the LH region, at several frequencies. The widest deep radio survey so far consists of a 6.6 deg². 1.4 GHz mosaic obtained with the Westerbork (WSRT) telescope (1σ sensitivity $\sim 10 \mu\text{Jy beam}^{-1}$; Prandoni et al. 2018). We refer to Prandoni et al. (2018) for a comprehensive summary of the available multi-frequency and multi-band coverage in this region (see also Kondapally et al. 2020, paper III of this series).

The Boötes (Boo hereafter) field was originally targeted as part of the NOAO Deep Wide Field Surveys (NDWFS; Jannuzi & Dey 1999) which covers ~ 9 deg² in the optical and near infrared (K) bands. Ancillary data is available for this field including X-ray (Murray et al. 2005; Kenter et al. 2005), UV (GALEX; Martin et al. 2003), and mid-infrared (Eisenhardt et al. 2004). Radio observations have also been carried out at 153 MHz with the GMRT (Intema et al. 2011; Williams et al. 2013), at 325 MHz with the VLA (Croft et al. 2008, Coppejans et al. 2015) and at 1.4 GHz with the WSRT (de Vries et al. 2002).

The Elais-N1 (EN1 hereafter) field has deep multi-wavelength ($0.15\mu\text{m} - 250\mu\text{m}$) data taken as part of many different surveys (optical: the Panoramic Survey Telescope and Rapid Response System; Pan-STARRS (Chambers et al. 2016) and Hyper-Suprime-Cam Subaru Strategic Program (HSC-SSP) survey, u-band: Spitzer Adaptation of the Red-sequence Cluster Survey; SpARCS: Muzzin et al. 2009, UV: Deep Imaging Survey (DIS): Martin et al. 2005, NIR J and K band: the UKIDSS Deep Extragalactic Survey (DXS) DR10 (Lawrence et al. 2007), MIR: IRAC instrument on board the Spitzer Space Telescope: SWIRE; Lonsdale et al. 2003 and The Spitzer Extragalactic Representative Volume Survey (SERVS; Mauduit et al. 2012).

Mahony et al. (2016) presented the first LOFAR 150 MHz map of the LH

Table 5.1: An overview of the statistical properties of the three LoTSS Deep Fields.

Field	R.A. (hh:mm:ss)	DEC. (dd:mm:ss)	Obs. Time (hr)	σ_c ($\mu\text{Jy beam}^{-1}$)	Area _{full} (deg ²)	N_S^{raw}	$\sigma_{\text{med}}^{\text{full}}$ ($\mu\text{Jy beam}^{-1}$)	Area _{masked} (deg ²)	N_S^{final}	$\sigma_{\text{med}}^{\text{masked}}$ ($\mu\text{Jy beam}^{-1}$)
LH	10:47:00.0	+58:04:59.0	112	22	25.0	50112	40	10.3	31162	29
Boo	14:32:00.0	+34:30:00.0	80	32	26.5	36767	58	8.6	19179	42
EN1	16:11:00.0	+55:00:00.0	164	17	24.3	69954	31	6.7	31610	21

Notes: the columns are as follows: pointing centre (R.A. and DEC); total observing time; RMS noise reached at the center of the image (σ_c); area covered by the raw catalogue (Area_{full}), number of sources in the raw catalogue (N_S^{raw}) and median RMS noise in the area covered by the raw catalogue ($\sigma_{\text{med}}^{\text{full}}$); same parameters for the final catalogue (Area_{masked}, N_S^{final} , $\sigma_{\text{med}}^{\text{masked}}$).

with a sensitivity of $160 \mu\text{Jy beam}^{-1}$ at a resolution of $18.7'' \times 16.4''$. [Williams et al. \(2016\)](#) presented the first LOFAR map of the Boo field at a resolution of $5.6'' \times 7.4''$ with an rms of $120 \mu\text{Jy beam}^{-1}$. A deeper image of the Boo field, reaching an rms of $55 \mu\text{Jy}$ at its center, was presented by [Retana-Montenegro et al. \(2018\)](#). Tasse et al. (2020, paper I) present the deepest, high-resolution ($6''$) low-frequency images and catalogues of the LH and Boo fields at 150 MHz and also describe the general method followed for the data reduction of the LoTSS Deep Fields. The even deeper LOFAR observations of the EN1 field are presented separately by Sabater et al. (2020, paper II).

One of the immediate science products of deep radio surveys is the determination of the radio source counts, which can provide useful comparison with counts predictions based on evolutionary models of radio source populations. In the present paper, we collectively exploit the LH, Boo and EN1 deep LOFAR data to derive the deepest radio source counts at 150 MHz ever. The derived source counts are compared with other existing determinations, as well as with state-of-the-art radio source evolutionary models (e.g. [Wilman et al. 2008](#); [Mancuso et al. 2017](#); [Bonaldi et al. 2019](#)).

The outline of the paper is as follows. In Section 2 the data reduction and the imaging process followed to obtain the deep images of the LH, Boo and EN1 are described in brief. In Section 3, we summarize the source extraction process and we describe the derived source catalogues and corresponding properties. This is followed by an analysis of the source size distribution and of the catalogue incompleteness due to resolution bias (Section 4). Eddington bias and related incompleteness are discussed in Section 5. Section 6 presents the derived 150 MHz source counts and their comparison with state-of-the-art evolutionary models. We summarize our results in Section 7. Throughout this paper, we have used the convention $S_\nu \propto \nu^\alpha$.

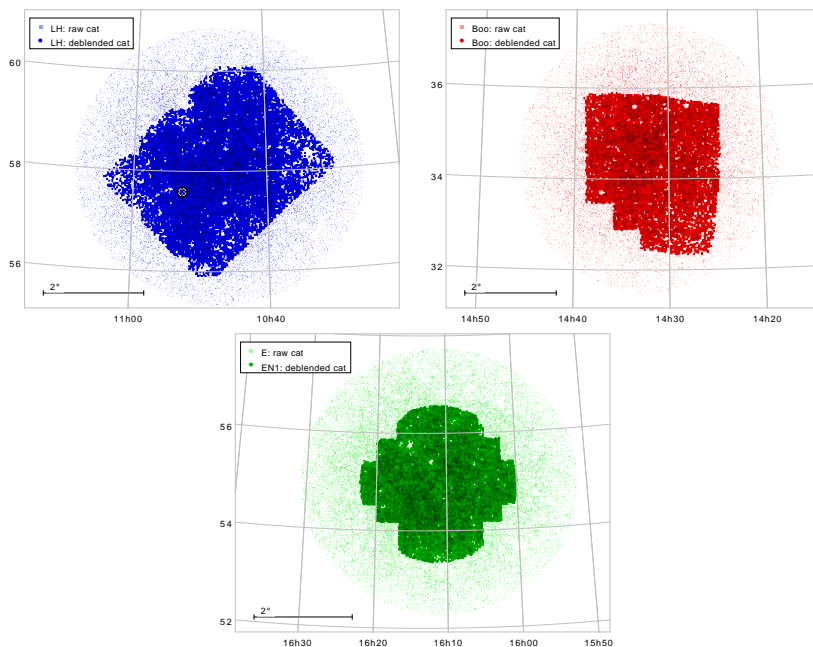


Figure 5.1: LH (top left), Boo (top right) and EN1 (bottom) fields targeted by LOFAR at 150 MHz. Light colors refer to the raw catalogues, cut at a distance from the pointing center of 0.3 of the LOFAR 150 MHz primary beam power. Darker colors refer to the final catalogues. The varying shape of their footprints highlights the regions with available optical/IR data. The areas of the optical/IR footprints are listed in Table 5.1.

5.2 Observations and Data reduction

The observations and data reduction of the LoTSS Deep Fields are described in detail in paper I, but for completeness we provide a brief summary below.

Each of the deep fields was observed using the LOFAR High Band Antenna (HBA) in its HBA_DUAL_INNER mode. Observations were taken in approximately 8hr blocks and the total integration times were 112, 80 and 164 hours for the LH, Boo and EN1 fields respectively¹. The phase centers of the three pointings are listed in Table 5.1 (R.A., DEC.). The calibration of the data was completed in two steps. Firstly a direction independent calibration was performed using the PREFACTOR pipeline² which is described in [van Weeren et al. \(2016a\)](#) and [Williams et al. \(2016\)](#) and corrects for direction independent effects (see [de Gasperin et al. 2019](#)). To efficiently deal with the large data rates, this pipeline is run on a compute cluster connected to the LOFAR archive (see [Mechev et al. 2018](#) and [Drabent et al. 2019](#)). The resulting data products are then calibrated with the latest version of DDF-PIPELINE³ which is briefly outlined in Section 5.1 of [Shimwell et al. 2019](#) and detailed by paper I. This pipeline is based on the kMS solver ([Tasse 2014](#); [Smirnov & Tasse 2015](#)) and the DDFacet imager ([Tasse et al. 2018](#)) to calibrate for direction-dependent effects, such as ionosphere-induced and beam model errors, and apply these solutions whilst imaging.

As described in [Tasse et al. \(2018\)](#), for each deep field a single good observation is selected and run through DDF-PIPELINE. The resulting sky model, together with all observations from that particular field, are then input into a second run of DDF-PIPELINE which calibrates all the data off that sky model, before imaging all the data together and completing a final round of direction independent and direction-dependent self-calibration. The frequency coverage used to produce the images is 120 MHz to 168 MHz for Boo and LH and 115 MHz to 177 MHz for EN1⁴.

As described in papers I and II, the peak and integrated flux densities of the final images were rescaled by factors of 0.920, 0.859 and 0.796 for the LH, Boo and EN1 fields respectively. These scaling factors were derived from the comparison of the LOFAR flux densities with a variety of shallower radio surveys available at various frequencies over these fields. The minimum sensitivity

¹A full overview of the observation details is given in Table 1 of paper I (for the LH and the Boo fields) and in Table 1 of Paper II (for the EN1 field).

²<https://github.com/lofar-astron/prefactor>

³<https://github.com/mhardcastle/ddf-pipeline>

⁴The exact central frequency of the imaged band is therefore 144 MHz for LH and Boo, and 146 MHz for EN1.

reached at the center of the images (after rescaling) is $\sigma_c \sim 22, 32, 20 \mu\text{Jy beam}^{-1}$, respectively, at a resolution of $6''$ (see Table 5.1). Although dynamic range effects are present around bright sources, in all cases the final image noise levels are within $\sim 10\%$ of the noise levels predicted from 8-hr depths, assuming an rms scaling with time $t^{-0.5}$. We note that the noise measured in the Boo field is higher compared to the other two, also due to its lower declination.

5.3 Source extraction, masking and deblending

Initial source catalogues were extracted in each field using the PYthon Blob Detector and Source Finder (PYBDSF: Mohan & Rafferty 2015). The strategy followed for LH and Boo is detailed in paper I. In brief, the source detection threshold was set at 5σ for the peak flux and at 3σ for the definition of the contiguous pixels used for the source Gaussian fitting, where σ is defined as the local rms noise at the source position. To measure the background noise variations across the images, a sliding box of the size of 40×40 synthesized beams was used. For high signal-to-noise (≥ 150) sources, the box size was reduced to 15×15 synthesized beams in order to capture the increased local noise level more accurately. For EN1 a slightly different set of parameters was used (see Table C.1 of paper II). The PyBDSF wavelet decomposition mode was used in all fields to better describe complex sources characterized by very extended emission. A flag is assigned to each source according to the number of Gaussian components fitted: ‘S’ and ‘M’ refer to sources fitted by a single and multiple Gaussian components respectively, whereas ‘C’ means that the source lies within the same island as another source. For a more detailed description of the method and format of the catalogues, see the webpage⁵ and Shimwell et al. (2019). The catalogues were cut at a distance from the pointing centre roughly corresponding to 0.3 of the 150 MHz LOFAR primary beam power (corresponding to fields of view of about 25 deg^2). The footprints of these initial catalogues (hereafter referred to as *raw* catalogues) are shown in light colors in Figure 5.1. The total number of sources over these footprints is respectively 50, 112 (LH), 36, 767 (Boo) and 69, 954 (EN1).

Deep and wide optical and IR data are available over part of the LoTSS Deep Fields. Over these common sub-regions, we could carry out an extensive process of multi-wavelength cross-matching and source characterisation, that allowed us to produce a cleaner and more reliable radio source catalogue. This

⁵<http://www.astron.nl/citt/pybdsf/>

process is extensively described by paper III, and only briefly reported here. Using a combination of statistical techniques and visual cross-matching, distinct PyBDSF components belonging to the same physical radio sources were grouped together to form multiple-component and/or complex radio sources. In addition, PyBDSF components were identified that needed to be deblended into separate Gaussian components associated with different host galaxies. In the same process, using the deep multi-wavelength datasets we were able to identify the host galaxies of over 97% of the detected radio sources⁶. After masking, the catalogues cover respectively 10.3 deg² (LH), 8.6 deg² (Boo) and 6.7 deg² (EN1), and collect respectively 31,163 (LH), 19,179 (Boo) and 31,645 (EN1) sources. In the following we will refer to these deblended/associated catalogues as *final* catalogues. The footprints of the final catalogues are shown in dark colors in Figure 5.1. The irregular shape of these footprints follows the optical/IR sky coverage. We note that ‘holes’ are present in such footprints, due to the fact that regions with very bright optical and/or radio sources (which typically produce artifacts in their surroundings) were masked.

In addition we have pixel-matched the images in each waveband and extracted aperture-matched photometry from ultraviolet to infrared wavelengths, deriving high-quality photometric redshifts for around 5 million objects across the three fields (see Duncan et al., 2020, paper IV of this series, for more details). The raw and final radio catalogues, as well as the optical/IR and photometric catalogues, are available on the LOFAR Surveys Data Release site web-page⁷.

5.3.1 Visibility function of raw and final catalogues

Figure 5.2 shows the so-called visibility function (i.e. the cumulative fraction of the total area of the noise map characterized by noise measurements lower than a given value) for the LH (blue), Boo (red) and EN1 (green) fields. Raw and final catalogues are indicated respectively by the dashed and solid lines. We note that the visibility functions of final catalogues are significantly steeper than those of the raw catalogues. This is due to the fact that the final catalogues are mostly confined in the inner, most sensitive parts of the LOFAR fields. As a consequence the median noise is significantly lower for final than for raw catalogues (see Table 5.1).

⁶97.6% for EN1 and LH; 96.9% for Boo.

⁷<http://www.lofar-surveys/releases.html>

Table 5.2: Parameters describing the unresolved/resolved sources' dividing lines (see Eqs. 5.2 and 5.3) for the LH, Boo and EN1 catalogues.

Field	A	B	% _{resolved}	
			raw	final
LH	1.15	3.0	34	25
Boo	1.00	2.0	47	38
EN1	1.07	3.0	35	24

5.3.2 Source Size Deconvolution

Characterisation of resolved versus unresolved sources in our catalogues is important in order to correct the catalogues for the incompleteness introduced by so-called *resolution bias* (described in Section 5.4). The total flux density (S_{total}) of a source can be written as:

$$S_{\text{total}}/S_{\text{peak}} = \theta_{\text{maj}}\theta_{\text{min}}/b_{\text{min}}b_{\text{maj}} \quad (5.1)$$

where S_{peak} is the source peak flux density, θ_{min} and θ_{maj} are the source full-width-half-maximum (FWHM) axes, and b_{min} and b_{maj} are the restoring beam FWHM axes. In an ideal image, in the absence of noise, the total flux density of a point source is equal to its peak flux density. In real images both the total and peak flux measurements of point sources are affected by errors. This means that not all sources with $S_{\text{total}} > S_{\text{peak}}$ would be genuinely resolved sources. The $S_{\text{total}}/S_{\text{peak}}$ ratio as a function of signal-to-noise ratio ($\text{SNR} = S_{\text{peak}}/\sigma$, where σ is the local rms noise), can be used to establish a statistical criterion to establish if a source is likely extended or point-like (see e.g. Prandoni et al. 2000b, 2006). In Figure 5.2, the ratio of the total to peak flux densities is shown as a function of SNR for both raw and final catalogues. A lower envelope of the source distribution can be defined by the following equation:

$$S_{\text{total}}/S_{\text{peak}} = A/(1 + B/\text{SNR}) \quad (5.2)$$

where A and B are two free parameters (see dashed lines in each panel of Fig. 5.2). As expected, going to higher SNR, measurement errors get smaller. At $\text{SNR} \gg 100$ the 2nd term of Eq. 5.2 can be neglected, and the $S_{\text{total}}/S_{\text{peak}}$ tends to A. In an ideal case, where radial smearing is taken care of, the ratio of the total over the peak flux density for point sources should converge to a value

of $A=1$ at very high SNRs. The DDFacet pipeline implements a facet dependent PSF which, for deconvolved sources, accounts for the impact of time and bandwidth smearing (Tasse 2014). However, due to imperfect calibration of the PSF across the field and/or smearing of sources due to ionospheric distortions, the value of the ratio at high signal-to-noise sources can be found to be higher than 1 and can be field-dependent (as ionospheric effects are time and spatially dependent). The values of A for the LH, Boo and EN1 field are respectively 1.15, 1.00 and 1.07 (see Table 5.2). This could potentially mean that the Boo field is less affected by ionospheric smearing when compared with LH and EN1. The B value also changes depending on the field, with Boo showing a lower value than LH and EN1 (see Table 5.2), again indicating smaller errors in the determination of source flux densities. We notice that the parameters given in Table 5.2 provides a good description of both raw and final catalogues. The lower envelopes can then be mirrored around the $S_{\text{total}}/S_{\text{peak}} = A$ axis to get the upper envelopes:

$$S_{\text{total}}/S_{\text{peak}} = A \cdot (1 + B/\text{SNR}) \quad (5.3)$$

Sources lying above the upper envelopes (dashed black lines in each panel) are then considered to be truly extended or resolved sources. Sources below the upper envelopes are considered to be point sources. The fraction of resolved sources in each field is given in Table 5.2. In final catalogues the fraction of resolved sources vary from 24-25% (EN1 and LH) to 38% (Boo). The $\sim 10\%$ higher fractions observed in raw catalogues reflect the larger number of bright extended sources detected in their larger FoV. These fractions should be considered as indicative, as they depend on the criteria used to define them. Sabater et al., for instance, as part of their detailed analysis of the EN1 field, used more stringent criteria, which also include additional sources of errors for the source fluxes, and estimated that between 4 and 11% of the sources in the EN1 raw catalogues are genuinely extended (see paper II for more details). Nevertheless, we decided to apply the same approach to all fields, and to both final and raw catalogues, to enable a consistent statistical analysis of the source size distribution in the three fields (see Sect. 5.4).

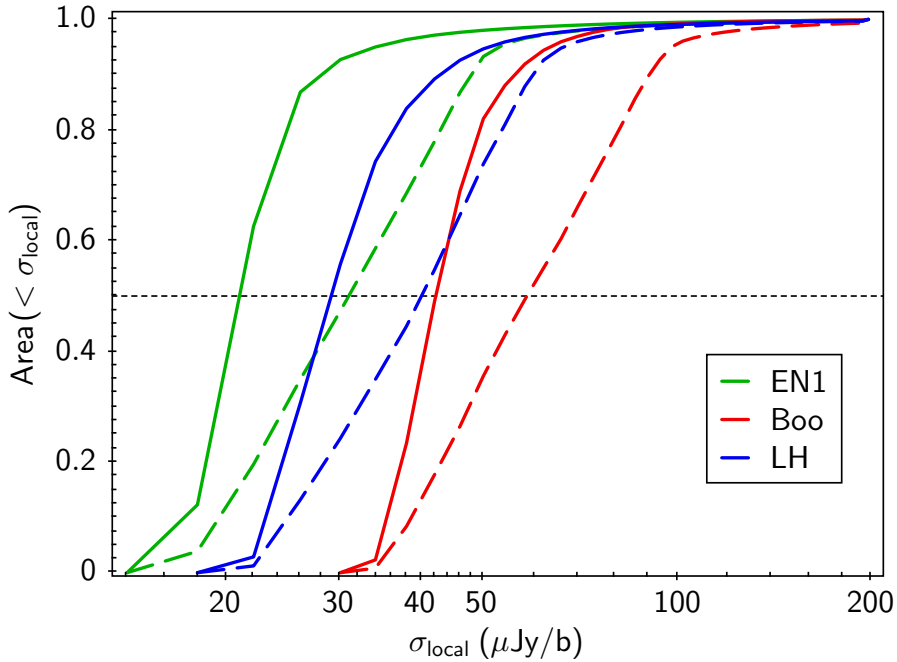
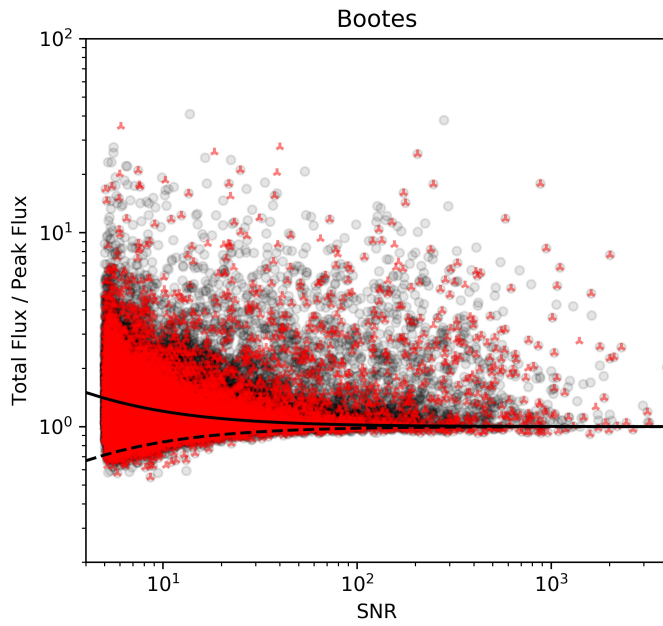
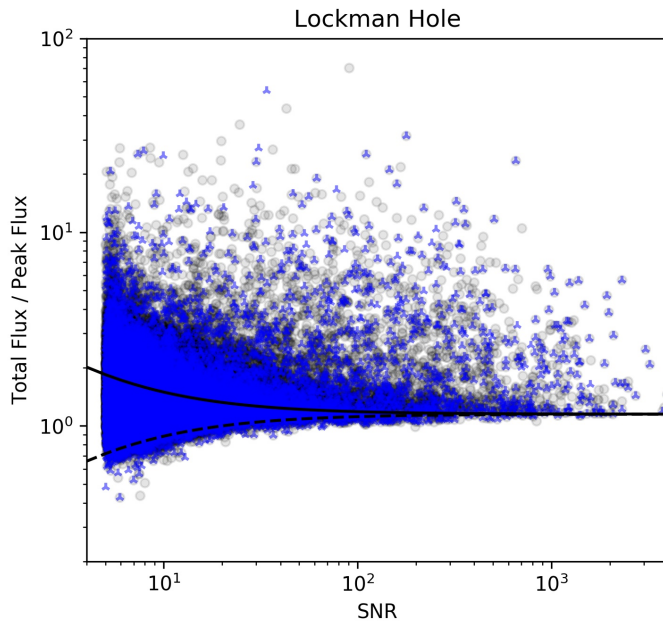


Figure 5.2: Visibility functions of the raw (dashed lines) and final (solid lines) catalogues presented in this paper. Blue, red and green colors correspond to the LH, Boo and EN1 fields, respectively. The visibility functions represent the cumulative fraction of the total area of the noise map characterized by a noise lower than a given value. We caveat that the total area covered by the final catalogues is much smaller than the one covered by the raw catalogues (see Tab. 5.1).



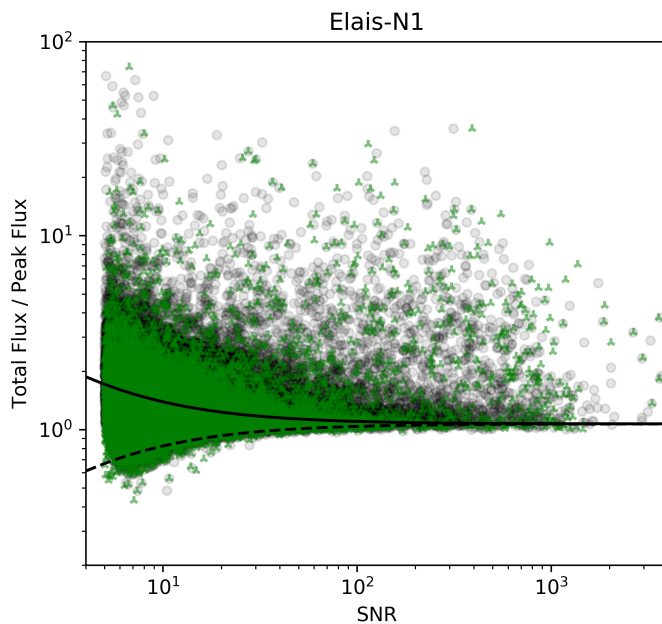


Figure 5.2: Total to peak flux density ratio as a function of signal to noise ratio ($\text{SNR} = S_{\text{peak}}/\sigma$) for both the raw (black transparent circles) and final (\blacktriangle symbols in blue, red and green colors) catalogues in the LH, Boo and EN1 fields (respectively from *top left* panel). The dashed and solid lines represent the unresolved source distribution lower and upper envelopes respectively (see text for more details).

5.4 Source Size Distribution and Resolution Bias

In deriving the source counts, the completeness of the catalogues in terms of total flux density needs to be estimated. Such completeness depends on source angular sizes, since, as shown by Eq. 5.1, a larger source of a given total flux density will drop below the 5σ limit of a survey more easily than a smaller source of the same total flux density. This effect, called *resolution bias*, results from the fact that the detection of a source depends on its peak flux. Following Prandoni et al. (2001b, 2006), we can use Eq. 5.1 to calculate the approximate maximum deconvolved size (Θ_{\max}) a source of a given total flux, S_{total} , can have before dropping below the 5σ limit of the catalogue:

$$\Theta_{\max} = \Theta_N \sqrt{(S_{\text{total}}/(5\sigma) - 1)} \quad (5.4)$$

where $\Theta_N \equiv \sqrt{b_{\text{maj}}b_{\text{min}}}$ is the geometric mean of the restoring beam axes. In our case $\Theta_N = b_{\text{maj}} = b_{\text{min}} = 6''$.

In Figure 5.3 we show the deconvolved source sizes as a function of the total flux density for both raw and final catalogues. Each panel corresponds to a different field: LH (top-left), Boo (top-right) and EN1 (bottom). Deconvolved sizes are defined as the geometric mean of the major and minor FWHM axes, except for well resolved radio galaxies, which are better described by their major axis. Deconvolved sizes of point sources are set to zero. As expected, the upper envelope of the source size distributions approximately follow the $\Theta_{\max} - S_{\text{total}}$ relation (short-long-dashed line) in all fields.

Equations 5.1 and 5.3 can also be used to derive an approximate minimum intrinsic angular size (Θ_{\min}) that can be resolved reliably as a function of the source peak flux density:

$$\Theta_{\min} = \Theta_N \sqrt{A \cdot (1 + B/\text{SNR}) - 1} . \quad (5.5)$$

The curve representing Θ_{\min} is shown in Figure 5.3 by the solid lines.

In order to quantify the fraction of sources larger than Θ_{\max} , and in turn the incompleteness affecting our catalogue, we need to know the true intrinsic radio source size distribution within the flux range probed by our survey. We start assuming the empirical integral distribution proposed by Windhorst et al. (1990) for 1.4 GHz-selected samples:

$$h(> \Theta) = \exp[-\ln 2 (\Theta/\Theta_{\text{med}})^q] \quad (5.6)$$

where $q = 0.62$ and the median source size varies with the total flux density as follows:

$$\Theta_{\text{med}} = k \times (S_{1.4\text{GHz}})^m \quad (5.7)$$

with $k=2''$, $m = 0.3$, $S_{1.4\text{GHz}}$ expressed in mJy. The [Windhorst et al. \(1990\)](#) relations are extensively used in the literature to estimate the resolution bias, either for 1.4 GHz selected samples (see e.g. [Prandoni et al. 2001b, 2018](#); [Huynh et al. 2005](#); [Hales et al. 2014b](#)), or for surveys at other frequencies, including LOFAR HBA ones ([Mahony et al. 2016](#); [Williams et al. 2016](#); [Retana-Montenegro et al. 2018](#)). We converted the median size - flux relation to 150 MHz assuming a spectral index $\alpha = -0.7$. This assumption is appropriate for radio catalogues dominated by faint sub-mJy radio sources. Indeed spectral index analyses performed using shallower ($S_{150\text{MHz}} \geq 1$ mJy) LOFAR observations of the Boötes and LH fields, report overall median spectral index values of $\alpha_{150\text{MHz}}^{1.4\text{GHz}} = -0.73 \pm 0.33$ and -0.78 ± 0.24 , for AGN and star-forming galaxies respectively (Boötes; [Calistro Rivera et al. 2017](#)), as well as a flattening of the spectral index going to lower flux densities, with a median value of $\alpha_{150\text{MHz}}^{1.4\text{GHz}} = -0.7^{+0.02}_{-0.04}$ at $S_{150\text{MHz}} \sim 1 - 2$ mJy (LH; [Mahony et al. 2016](#)).

As shown in Figure 5.3 the median sizes of both raw and final catalogues (respectively indicated by filled black-bordered magenta squares and golden circles with error bars) are compared with the [Windhorst et al. \(1990\)](#) size - flux relation converted to 150 MHz (long-dashed line). We see a discrepancy at intermediate fluxes (10 – 100 mJy), where the measured sizes appear in slight excess to what was predicted by [Windhorst et al. \(1990\)](#). We therefore decided to consider also the median size – flux relation derived from the Tiered Radio Extragalactic Continuum Simulation (T-RECS) catalogues at 150 MHz ([Bonaldi et al. 2019](#), dot-dashed line), which implement different size – flux scaling relations for star-forming galaxies and AGN. This seems to better reproduce our measured sizes at fluxes $S_{150\text{MHz}} \sim 10 - 100$ mJy, where extended radio galaxies (with typical sizes of hundreds of kpc) are expected to provide a significant contribution to the total radio source population. We caveat, however, that the afore-mentioned analysis is limited to flux densities $S_{150\text{MHz}} \geq 2$ mJy, while the large majority of the sources in the LoTSS Deep Fields are fainter. Most of these sources cannot be reliably deconvolved, implying that no direct information on their size distribution can be obtained. Several attempts have been made to estimate the intrinsic source sizes at sub-mJy fluxes, based on deep samples carried out over a wide range of observing frequencies (from 330 MHz to 10 GHz). Some of these works have proposed a steepening of the [Windhorst et al. \(1990\)](#) median size - flux relation at sub-mJy fluxes, with $m = 0.4 - 0.5$ in the range 0.1 – 1 mJy ([Richards 2000](#); [Bondi et al. 2003, 2008](#); [Smolčić et al. 2017](#)). A smooth transition from a flatter to a steeper relation at sub-mJy fluxes could again be justified by a smooth transition from a flux regime dominated by extended radio galaxies ($S \gg 1$ mJy) to a flux regime dominated by radio sources triggered by

star-formation (or by composite SF/AGN emission), confined within the host galaxy.

In order to establish which size–flux relation would best quantify the incompleteness of our catalogues we have decided to include in our analysis the results from other deep surveys. Figure 5.4 shows the existing measurements of (median) source sizes in various flux bins for a number of surveys (different colors/symbols refer to different observing frequencies). Also shown are the median sizes derived by combining together the three LoTSS fields (raw and final catalogues, respectively indicated by filled black-bordered magenta squares and golden circles). To make the comparison meaningful, all fluxes referring to a different observing frequency have been converted to 1.4 GHz, assuming $\alpha = -0.7$. Also shown are various size – flux relations: the ones proposed by [Bonaldi et al. \(2019\)](#), converted to 1.4 GHz) and [Windhorst et al. \(1990\)](#) (dot-dashed and long-dashed lines respectively), and some modifications of the latter. The short dashed lines show the ones obtained by rescaling the [Windhorst et al. \(1990\)](#) relation by $1.5\times$ and $2\times$ (i.e. assuming $k=3$ and $k=4$ in Eq. 5.7), while the dotted line assumes a smooth transition between $m = 0.3$ and $m = 0.5$ going from mJy to sub-mJy flux densities, i.e.:

$$m = m(S) = 0.3 + 0.2 \times \exp(-S_{1.4\text{GHz}}^2) \quad (5.8)$$

with $S_{1.4\text{GHz}}$ expressed in mJy. Focusing on the sub-mJy regime, it is clear that both the [Windhorst et al. \(1990\)](#) and the steeper $m(S)$ relations are consistent with the observed sizes, especially when considering only the 1.4 GHz surveys (black filled triangles). Surveys undertaken at higher frequencies seem to point towards the steeper relation, but these samples may be biased towards a flatter spectrum population, resulting in an over-estimation of the flux densities once converted to 1.4 GHz assuming a too steep spectral index. We also caveat that higher frequency surveys more easily miss extended flux, and resolution bias issues can indeed mimic a steepening of source median sizes getting close to the flux limit of a radio survey. At larger flux densities ($S_{1.4\text{GHz}} \geq 1$ mJy) the median sizes are observed to lie between the [Windhorst et al. \(1990\)](#) relations described by $k = 2$ and $k = 4$, with a tendency for larger sizes going to lower frequency. Indeed some source counts’ analyses of shallower LOFAR surveys in the LH and Boo fields claimed in the past a better consistency with a $k = 4$ [Windhorst et al. \(1990\)](#) median size – flux scaling relation ([Mahony et al. 2016](#); [Retana-Montenegro et al. 2018](#)). It is interesting to note, however, that the LoTSS final catalogues are characterized by smaller median sizes than the raw catalogues at their faint end ($S_{1.4\text{GHz}} \leq 5$ mJy), indicating that confusion significantly affects the measured sizes of the faintest sources, and that a significant

number of faint sources were deblended. On the other hand, the final catalogues tend to be characterised by larger sizes at the bright end ($S_{1.4\text{GHz}} \geq 100$ mJy), likely as a consequence of the association of multiple components into single sources, after visual inspection of the radio/optical images (see Sect 5.3). After accounting for these effects, LoTSS median sizes (golden filled circles) are consistent with the Windhorst et al. (1990) $k = 2$ size – flux relation up to $S_{1.4\text{GHz}} \sim 2$ mJy. Then they smoothly increase and become consistent with the Bonaldi et al. (2019) relation at $S_{1.4\text{GHz}} \geq 10$ mJy. At $S_{1.4\text{GHz}} \geq 100$ mJy the LoTSS source median sizes show large uncertainties. At these large flux densities also the Bonaldi et al. (2019) relation is poorly determined, being based on a simulated catalogue covering a similar area to the one covered by the LOFAR deep fields (25 deg²). It is interesting to note, however, that both are consistent with the Windhorst et al. (1990) relation. Based on all the above considerations, a good description of the observed median sizes can be obtained by the following analytical form, which assumes the Windhorst et al. (1990) relation with a varying $k = k(S)$, i.e.:

$$k = \begin{cases} 3.5 - 1.5 \times \exp(-S_{1.4\text{GHz}}/2) & S_{1.4\text{GHz}} < 4.5 \\ 2 + 1.5 \times \exp(-S_{1.4\text{GHz}}/200) & S_{1.4\text{GHz}} \geq 4.5 \end{cases} \quad (5.9)$$

where $S_{1.4\text{GHz}}$ is expressed in mJy (see solid line in Fig. 5.4).

Another important consistency check regards the angular size distribution of the sources. Figure 5.5 shows the cumulative size distributions of the final catalogues combined together, in four flux density bins (yellow solid lines). Such distributions can be considered reliable only down to a flux-dependent minimum intrinsic size (see vertical grey lines), below which most of the sources cannot be reliably deconvolved and they are conventionally assigned $\Theta = 0$. The observed distributions are compared with various realizations of the cumulative distribution function described by Eq. 5.6, obtained by varying either the function exponent q (left and right columns respectively) or the assumed median size – flux relations (see various black lines). The original function proposed by Windhorst et al. (1990) (Eq. 5.6 with $q = 0.62$, see left column) does provide a good approximation of the observed distributions, when assuming the original $\Theta_{\text{med}} - S$ relation described by Eq. 5.7, only at fluxes $S_{150\text{MHz}} \geq 10$ mJy (see long-dashed lines). This is perhaps not surprising considering that this relation was calibrated at 1.4 GHz down to a few mJy fluxes. At the lowest flux densities ($S_{150\text{MHz}} \leq 1$ mJy) we need to assume a steepening of the parameter m (see Eq. 5.8), to get a good match with observations (dotted line in the top left panel). This is consistent with what proposed for higher frequency deep surveys

(as discussed earlier in this Section). At intermediate fluxes ($S_{150\text{MHz}} \sim 1 - 10$ mJy, on the other hand, none of the discussed median size – flux relations can reproduce the observed size distribution (see second-row panel on the left). It is interesting to note, however, that if we assume a steeper exponent for the distribution function described by Eq. 5.7 (i.e. $q = 0.80$), we get a very good match with observations at all fluxes, when assuming a flux-dependent scaling factor ($k = k(S)$; see Eq. 5.9) for the Windhorst et al. (1990) median size – flux relation (black solid lines on the right). The median sizes derived from the T-RECS simulated catalogues (Bonaldi et al. 2019) also provide good results for $q = 0.80$ (dot-dashed lines on the right), except again at intermediate fluxes ($S_{150\text{MHz}} \sim 1 - 10$), where they show strong discrepancies with observations also in Fig. 5.4. This seems to indicate that the number density of extended radio galaxies in this flux density range is over-estimated in the T-RECS simulated catalogues.

Correction for Resolution Bias

The correction factor c that needs to be applied to the source counts to account for the resolution bias can be defined as (Prandoni et al. 2001b):

$$c = 1/[1 - h(> \Theta_{\text{lim}})] \quad (5.10)$$

where $h(> \Theta_{\text{lim}})$ takes the form of the integral of the angular size distribution proposed by Windhorst et al. (1990, see Eq. 5.6), and Θ_{lim} is the limiting angular size above which the catalogues are expected to be incomplete. Following Prandoni et al. (2001b), this is defined as:

$$\Theta_{\text{lim}} = \max[\Theta_{\text{min}}, \Theta_{\text{max}}] \quad (5.11)$$

where Θ_{max} and Θ_{min} are as defined in Eqs. 5.4 and 5.5 respectively. We notice that Θ_{lim} is always equal to Θ_{max} , except for the lowest flux bins, where Θ_{max} becomes unphysical (i.e. tends to zero). Θ_{min} accounts for the effect of having a finite restoring beam size (that is $\Theta_{\text{lim}} > 0$ at the survey limit) and a deconvolution efficiency which varies with the source peak flux (see Prandoni et al. 2001b for more details).

Figure 5.6 (left panel) shows the correction factor derived assuming the median size – flux relations discussed above, combined with appropriate values of the q exponent in Eq. 5.6, based on our analysis of the source size distribution (see Fig. 5.5 and related discussion). A caveat to keep in mind is that the resolution bias correction does depend on both the source flux and the noise

value at the source position (and/or the source signal-to-noise ratio; see Eqs. 5.4 and 5.5). The corrections presented in Fig. 5.6 (left panel) account for local and radial variations of the noise through empirical relations between source flux and local noise or signal-to-noise ratio, specifically derived for each field. Such relations describe average trends only, and hence the corrections presented here should be considered as indicative. The corrections effectively applied to the counts are based on the actual source flux, noise and signal-to-noise ratio distributions. It is interesting to note, however, that, as a consequence of radially-increasing noise (and/or limited dynamic range around bright radio sources), the correction factor c does not necessarily converge to 1 at large flux densities. As shown in Fig. 5.6, in the masked regions of our fields this only happens when assuming the shallower integral distribution function ($q = 0.62$). For the steeper one ($q = 0.80$), the expected number density of very extended sources is small, and resolution bias effects become negligible at $S_{150\text{MHz}} \geq 500$ mJy.

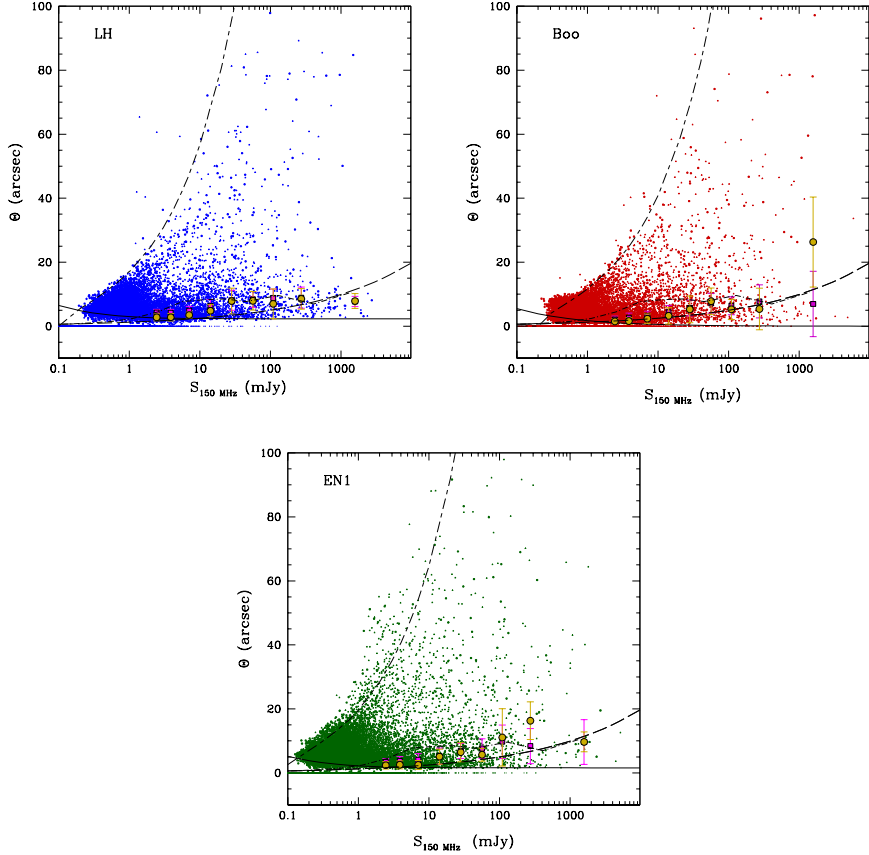


Figure 5.3: Source intrinsic (deconvolved) angular sizes as a function of the measured 150 MHz total flux densities. Deconvolved sizes are defined as the geometric mean of the major and minor FWHM axes, except for well resolved radio galaxies, which are better described by their major axis. Deconvolved sizes of point sources are set to zero. Raw (\cdot) and final (\wedge) catalogues of the LH, Boo and EN1 fields are shown in the top left, top right and bottom panels, respectively. The short-long-dashed lines in the three panels define the maximum size (Θ_{max}) a source can have for a given measured total flux before dropping below the detection threshold. The solid lines give the minimum size (Θ_{min}) below which deconvolution is not considered reliable. Both lines have been drawn assuming the median noise in the masked area (see last column of Table 5.1). The long-dashed lines indicate the Windhorst et al. (1990) median size - flux relation, converted to 150 MHz, while the dot-dashed lines indicate the median size - 150 MHz flux relation derived from the simulated T-RECS catalogues directly at 150 MHz (Bonaldi et al. 2019). The filled black-bordered magenta squares and golden circles with error bars represent the median source sizes for the raw and final catalogues respectively. Medians are computed only for those flux bins where unresolved sources represent less than 50% of the total number of sources.

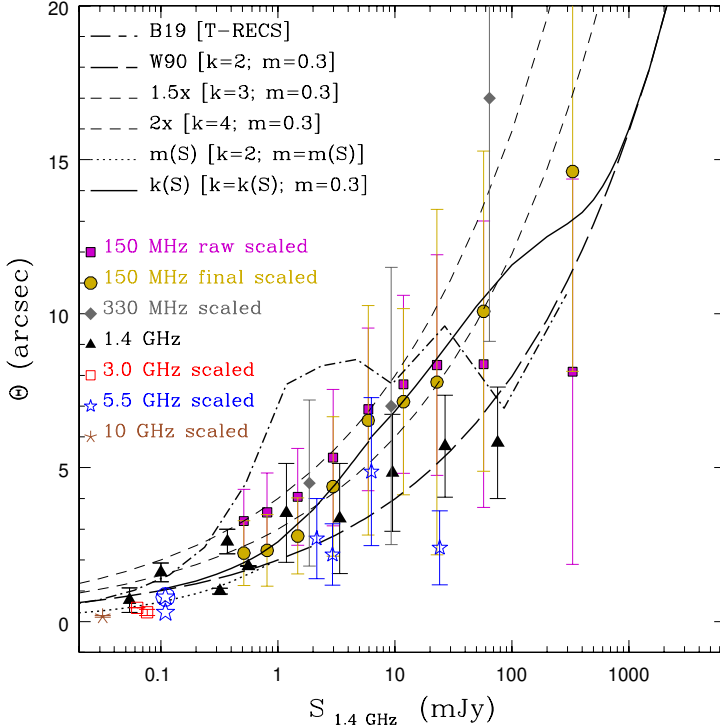


Figure 5.4: Source median angular size vs. 1.4 GHz total flux density, as estimated in some of the deepest radio samples available so far. Different colors/symbols correspond to different observing frequencies: 330 MHz (grey filled diamonds - Owen et al. 2009); 1.4 GHz (black filled triangles - Richards 2000; Bondi et al. 2003, 2008; Muxlow et al. 2005; Prandoni et al. 2018); 3 GHz (red empty squares - Bondi et al. 2018; Cotton et al. 2018); 5.5 GHz (blue stars - Prandoni et al. 2006; Guidetti et al. 2017); 10 GHz (brown asterisks - Murphy et al. 2017). Also shown are the median sizes measured in our raw and final catalogues (150 MHz), combined together (filled black-bordered magenta squares and golden circles). We note that Guidetti et al. (2017) gives different median sizes for the AGN and star-forming galaxy sub-populations. The latter population is indicated as a circled blue star in the figure. All fluxes have been converted to 1.4 GHz, assuming a spectral index $\alpha = -0.7$. Various median size – flux relations are shown for comparison: the ones proposed by Bonaldi et al. (2019) and Windhorst et al. (1990) (dot-dashed and long-dashed lines respectively), and some revised versions of the latter. The short dashed lines show the relations obtained by rescaling the Windhorst et al. (1990) relation by $1.5\times$ and $2\times$ (i.e. assuming $k = 3$ and $k = 4$ in Eq. 5.7); the dotted line assumes a smooth transition between $m = 0.3$ and $m = 0.5$ going from mJy to sub-mJy flux densities, as described by Eq. 5.8; the solid line assumes a value of k varying with flux density according to Eq. 5.9 (see text for more details).

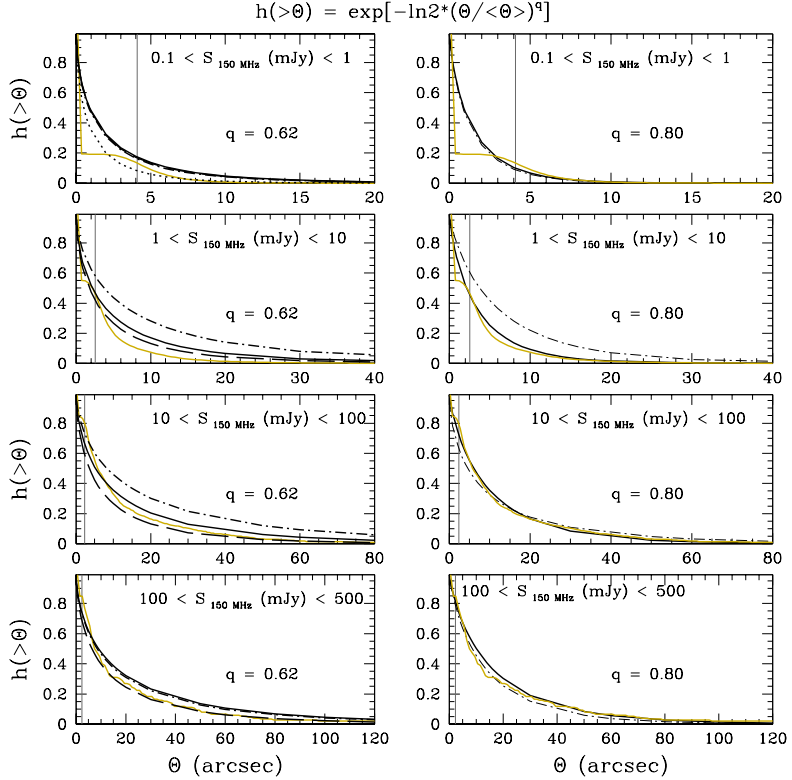


Figure 5.5: Source size cumulative distribution of final catalogues (yellow solid line) in four 150 MHz flux density bins. The vertical grey lines in all panels provides an approximate indication of the minimum intrinsic angular size to which the observed distributions can be considered reliable (most of the sources below this line cannot be reliably deconvolved and they are conventionally assigned $\Theta = 0$). Also shown for comparison are various realizations of the cumulative distribution function described by Eq. 5.6. The two columns correspond to two different values for the function exponent q : the original one proposed by Windhorst et al. (1990) ($q = 0.62$) on the left, and a steeper one ($q = 0.80$) on the right. In addition we also vary the median size – flux relation. In particular we assume the original Windhorst et al. (1990) relation (black long-dashed line), the revised versions with flux-dependent m and k parameters, as described by Eqs. 5.8 and 5.9 (black dotted and solid lines respectively) and the one describing the T-RECS catalogues (Bonaldi et al. 2019; black dot-dashed line). All such realizations are shown on the left; on the right we only show the realizations obtained using the Bonaldi et al. (2019) and the revised Windhorst et al. (1990) $k = k(S)$ relations.

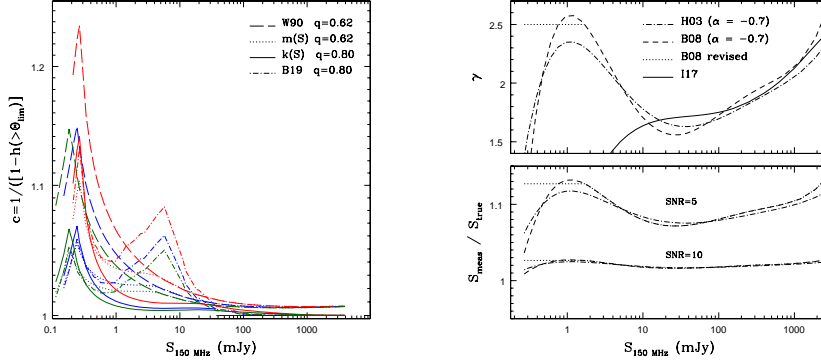


Figure 5.6: *Left*: Flux-dependent correction to be applied to source counts to account for incompleteness due to resolution bias, for four median size - flux relations: the one derived from the simulated T-RECS catalogues (Bonaldi et al. 2019; dot-dashed lines), the one proposed by Windhorst et al. (1990, long-dashed lines), the revised version with $m = m(S)$, which better describe source sizes at 1.4 GHz sub-mJy fluxes (see Eq. 5.8, dotted lines), and the revised version with $k = k(S)$ proposed by us (Eq. 5.9, solid lines). We also vary the q exponent of the integral distribution function. Based on our analysis of the source size distribution (see Fig. 5.5 and related discussion), we assume the original value proposed by Windhorst et al. (1990, $q = 0.62$) for the Windhorst et al. (1990) median size - flux relation and for the revised version with $m = m(S)$. We assume a steeper $q = 0.80$ for the revised version with $k = k(S)$ and for the Bonaldi et al. (2019) relation (see legenda). Different colors refer to different fields: LH (blue), Boo (red), EN1 (green). The corrections account for noise variations in the masked images through an empirical relation between source flux and source signal-to-noise ratio, calibrated for each field (we assume here the median noise of the masked images; see last column of Tab. 5.1). *Right*: Eddington bias for different underlying number-count distributions, as illustrated in the top panel: source counts' slope (γ ; $dN/dS \sim S^{-\gamma}$) derived from the sixth-order polynomial fit proposed at 1.4 GHz by a) Hopkins et al. (2003) (dot-dashed line) and b) Bondi et al. (2008) (dashed line), both converted to 150 MHz assuming a spectral index $\alpha = -0.7$; we also show a revised version of the Bondi et al. (2008) fit, which assumes a constant Euclidean slope ($\gamma = 2.5$) from 2 mJy all the way down to 0.1 mJy (dotted line). The polynomial fit proposed by Intema et al. (2017) at 150 MHz and valid only for the bright end of the counts is also shown for reference (solid line). The flux boosting ($S_{\text{meas}}/S_{\text{true}}$) corresponding to the three cases illustrated above is shown in the bottom panel for two different source signal-to-noise ratios: SNR=5 and SNR=10.

5.5 Eddington bias

While correcting for resolution bias is important to account for missed resolved sources, Eddington bias (Eddington 1913, 1940) should be taken into account to get an unbiased census of unresolved sources. Due to random measurement errors the measured peak flux densities will be redistributed around their true value. In presence of a source population which follows a non-uniform flux distribution, this will result in a redistribution of sources between number-count flux density bins. The way the sources are redistributed depends on the slope of source counts. If the source number density increases with decreasing flux, the fluxes tend to be boosted and the probability to detect a source below the detection threshold is higher than the probability to miss a source above the threshold, artificially boosting the detection fraction. As a consequence the catalogue incompleteness at the detection threshold is also biased.

There are two main approaches to correct for Eddington bias, both requiring an assumption about the true underlying source counts distribution (see Hales et al. 2014b for a full discussion): one can build the source counts using the boosted fluxes and then apply a correction to each flux bin, or one can correct the source fluxes, before deriving the counts. As demonstrated by Hales et al. (2014a) the two approaches give very similar and consistent results, and we decided to follow the latter approach. A maximum likelihood solution for the true source flux can be defined as follows (see Hales et al. 2014b and references therein):

$$S_{\text{true}} = \frac{S_{\text{meas}}}{2} \cdot \left(1 + \sqrt{1 - \frac{4\gamma}{\text{SNR}^2}} \right) \quad (5.12)$$

where $\gamma = \gamma(S)$ is the slope of the counts at the given flux density ($dN/dS \sim S^{-\gamma}$), and SNR is the source signal-to-noise ratio. The slope of the counts can be modeled from empirical polynomial fits of the observed counts:

$$\log \left(\frac{dN(S)}{dS} S^{2.5} \right) = \sum_{i=0}^n a_i (\log S)^i . \quad (5.13)$$

It is then easy to demonstrate that:

$$\gamma = 2.5 - \sum_{i=0}^n i \cdot a_i (\log S)^{i-1} . \quad (5.14)$$

In order to derive γ we can use one of the several counts' fits available in the literature. Intema et al. (2017) derived a fifth-order polynomial fit which describes

the 150 MHz normalized counts of the TIFR GMRT Sky Survey (TGSS), but this fit is only valid down to a flux limit of 5 mJy. The deepest fits available in the literature have been obtained at 1.4 GHz. We start by exploring the sixth-order ($n = 6$) polynomial fits obtained by Hopkins et al. (2003) and Bondi et al. (2008) for 1.4 GHz normalized source counts (converted to 150 MHz using $\alpha = -0.7^8$). The two cases are illustrated in the top right panel of Fig. 5.6 (dot-dashed and dashed lines respectively), where the derived counts' slope is shown. Both cases are consistent with the Intema et al. 150 MHz fit (indicated by the solid line) at bright flux densities ($S > 100$ mJy), while significant discrepancies are observed at fainter fluxes, where the deeper 1.4 GHz fits better describe the well-known flattening of the normalized counts. Both the 1.4 GHz fits show an increasing slope below 10 mJy, reaching a maximum around 1 mJy. This maximum is more pronounced in the case of Bondi et al. (2008), and is consistent with an Euclidean slope of $\gamma \sim 2.5$. At $S < 1$ mJy both slopes show a rapid drop. The reality and strength of this drop is unclear, as this is the flux regime where the fits are less reliably constrained. We then explore a third case, i.e. a modification of the Bondi et al. fit, which assumes a constant Euclidean slope at flux densities $S < 2$ mJy. This represents an extreme scenario, which however might be favoured by the recent 150 MHz source counts modeling proposed by Bonaldi et al. (2019), that indicates a flatter slope in the flux range 0.1 – 1 mJy. This last case is illustrated by the dotted line in Fig. 5.6 (top right panel). The flux boosting expected for the three aforementioned scenarios is illustrated in the bottom right panel of Fig. 5.6 for two signal-to-noise ratio values, SNR=5 and SNR=10.

Once the point source fluxes are corrected for Eddington bias, we can obtain an estimate of the catalogue incompleteness at the detection threshold through the use of Gaussian Error Functions (ERF).

⁸We caveat that assuming a single spectral index is a crude approximation. In principle we should account for the intrinsic scatter in the spectral index distribution of the sources, as well as for possible deviations of the mean spectral index with flux density, due to the varying relative contribution of the individual source populations. Such an approximation is however acceptable, since the largest uncertainties in this analysis come from the assumptions on the counts' slope at the faintest fluxes, which is very poorly known.

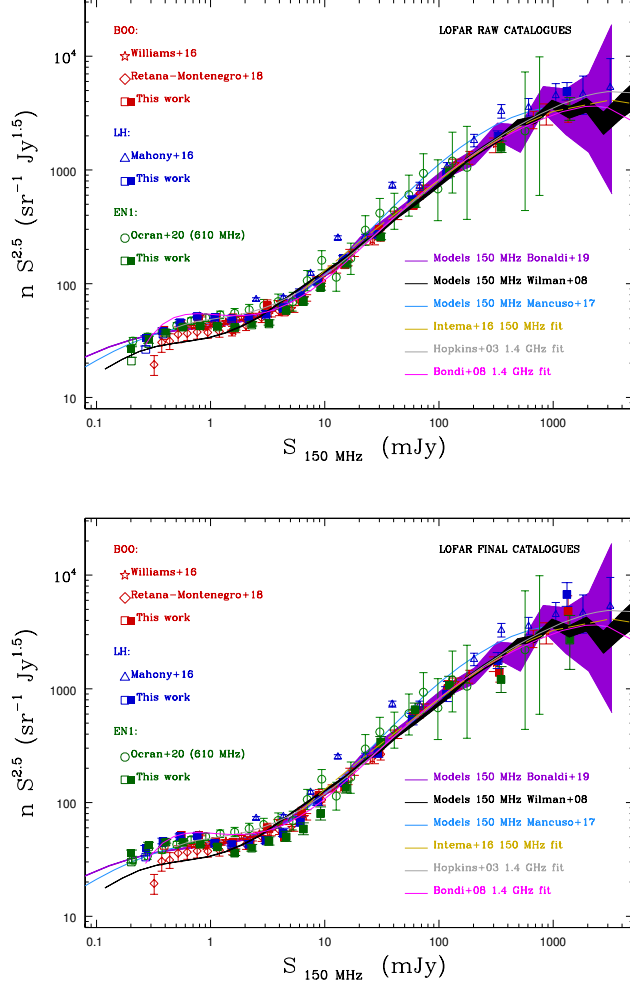


Figure 5.7: Normalized 150 MHz differential source counts in the three LoTSS Deep Fields, as derived from raw (*top*) and final (*bottom*) catalogues (filled squares). Error bars correspond to the quadratic sum of Poisson and systematic errors. Also shown are the counts obtained without applying the corrections discussed in Sects. 5.4 and 5.5 (empty squares). The counts are derived by using total flux densities for both point and extended sources. In both figures, Wilman et al. (2008), Bonaldi et al. (2019) and Mancuso et al. (2017) 150 MHz models are shown for comparison, as well as other existing 150 MHz counts’ determinations in the same fields (see legend). Since published 150 MHz counts are missing for EN1, we show a recent determination obtained at 610 MHz (Ocran et al. 2020) and rescaled to 150 MHz, assuming $\alpha = -0.7$. Also shown are the counts’ best fits discussed in Sect. 5.5.

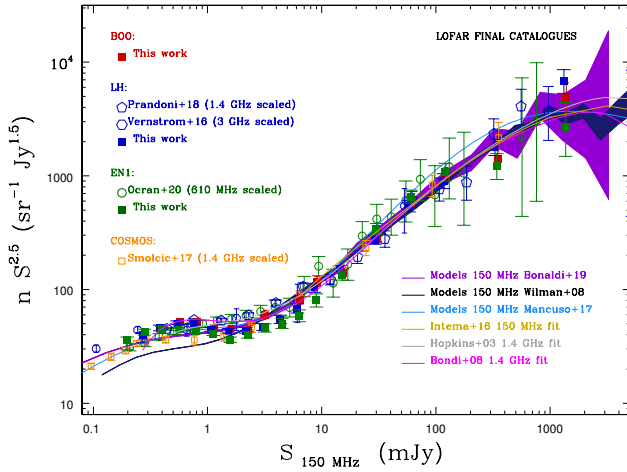


Figure 5.8: Normalized 150 MHz differential source counts in the three LoTSS Deep Fields, as derived from final catalogues (filled squares), compared to counts derived from higher frequencies surveys (see legend), and rescaled to 150 MHz by assuming $\alpha = -0.7$. Error bars correspond to the quadratic sum of Poisson and systematic errors. Also shown are the Wilman et al. (2008), Bonaldi et al. (2019) and Mancuso et al. (2017) 150 MHz models and the counts' best fits discussed in Sect. 5.5. The counts are derived by using total flux densities for both point and extended sources.

Table 5.3: 150 MHz normalized differential radio-source counts as derived from combining the raw and final catalogues of the three LoTSS Deep Fields. $\langle S \rangle$ is the geometric mean of the respective flux density bin, expressed in mJy; $N(\text{raw})$ and $N(\text{final})$ indicates the normalized source counts obtained from the raw and final catalogues respectively (in $Jy^{1.5}sr^{-1}$); $\pm\sigma_{\text{tot}}$ are the total errors on the counts, estimated as the quadratic sum of Poissonian and systematic errors. We note that only EN1 and LH sources contribute to the first flux density bin.

$\langle S \rangle$	$N(\text{raw})^{+\sigma_{\text{tot}}}_{-\sigma_{\text{tot}}}$	$N(\text{final})^{+\sigma_{\text{tot}}}_{-\sigma_{\text{tot}}}$
0.20	$26.20^{+1.53}_{-4.26}$	$32.88^{+2.10}_{-6.56}$
0.29	$34.00^{+2.053}_{-7.124}$	$40.56^{+2.52}_{-7.98}$
0.41	$38.94^{+2.47}_{-2.64}$	$45.74^{+2.78}_{-2.29}$
0.57	$44.80^{+2.78}_{-1.42}$	$49.64^{+2.61}_{-1.11}$
0.81	$49.19^{+2.78}_{-1.44}$	$48.78^{+2.30}_{-0.96}$
1.15	$48.39^{+2.44}_{-2.05}$	$43.40^{+1.78}_{-1.25}$
1.62	$47.86^{+2.82}_{-2.92}$	$42.36^{+1.97}_{-1.84}$
2.29	$48.47^{+3.55}_{-3.58}$	$41.74^{+2.34}_{-2.36}$
3.24	$55.72^{+4.69}_{-5.32}$	$51.93^{+3.42}_{-3.72}$
4.59	$60.25^{+5.89}_{-5.88}$	$52.30^{+4.32}_{-4.16}$
6.49	$79.17^{+7.88}_{-8.14}$	$73.08^{+5.65}_{-6.59}$
9.17	$104.4^{+8.0}_{-8.4}$	$105.4^{+7.4}_{-7.2}$
15.4	$160.0^{+8.7}_{-8.2}$	$142.6^{+7.7}_{-7.3}$
30.9	$290.5^{+18.0}_{-17.0}$	$307.0^{+18.4}_{-17.4}$
61.7	$533.2^{+41.5}_{-38.6}$	$597.5^{+43.7}_{-40.8}$
123	$970.0^{+96.6}_{-87.9}$	$991.0^{+96.8}_{-88.4}$
349	1911^{+204}_{-185}	1660^{+190}_{-171}
1396	3915^{+890}_{-745}	4793^{+967}_{-822}

5.6 Differential source counts

The differential source counts, normalised to a non-evolving Euclidean model, obtained from the LoTSS Deep Fields are shown in Figure 5.7, together with other count determinations obtained in the same fields from previous low-frequency surveys (see legend). The top and bottom panels refer to counts derived from the raw and final catalogues, respectively (see filled boxes). The source counts obtained from the final catalogues are reported in tabular form in the Appendix (Tables 5.5, 5.6 and 5.7, for LH, Boo and EN1 fields respectively), and are also shown in Fig. 5.8, where they are compared to counts extrapolated from higher frequencies. In deriving the counts we applied a ‘fiducial’ model for the systematic corrections described in Sects. 5.4 and 5.5. Specifically we assumed the [Windhorst et al. \(1990\)](#) size – flux relation with $k = k(S)$ (Eq. 5.9), in combination with a ‘steep’ ($q = 0.80$ in Eq. 5.6) integral size distribution, to estimate the resolution bias, and we assumed the [Bondi et al. \(2008\)](#) source counts best fit to estimate the Eddington bias. The uncertainties associated with such assumptions are factored into systematic error terms (see Sys^- and Sys^+ columns in the counts’ tables), that are defined as the maximum discrepancy between the ‘fiducial’ counts and those obtained assuming the other discussed models (shown in Fig. 5.6). Also shown in Fig. 5.7 are the counts obtained from the three LoTSS fields before applying the corrections for resolution and Eddington bias (empty boxes). As expected such corrections are only relevant for the lowest flux density bins. We cut the source counts at a threshold of $\sim 7\sigma_{\text{med}}$, where systematic errors dominate over Poissonian (calculated following [Gehrels 1986](#)) by factors $\sim 5 - 10$.

The normalized 150 MHz source counts derived from the three LoTSS Deep Fields are in broad agreement with the counts obtained from previous low- and high- frequency radio surveys (see Figs. 5.7 and 5.8), and show the well known flattening at $S \leq \text{few mJy}$. However, when comparing the source counts derived from raw and final catalogues, we notice a very interesting feature: the latter show a much more pronounced drop at fluxes around a few mJy, which results in a more prominent ‘bump’ in the sub-mJy regime. For a more quantitative analysis of this feature we have combined the sources in the three fields and produced a combined version of the source counts. This allows us to smooth out field-to-field variations due to cosmic variance and/or residual systematics (like e.g. residual flux scaling issues, see Sect. 5.2), as well as reduce the scatter at bright fluxes, where Poissonian errors dominate. The combined counts derived from raw and final catalogues are shown in Fig. 5.9 and listed in Tab.5.3. We

Table 5.4: Coefficients for 7-th order polynomial function defined by Eq. 5.13, which best-fit the LoTSS and TGSS 150 MHz normalized source counts. The polynomial fit is shown in Figure 5.9.

Coefficient	Value	Error (\pm)
a_0	1.656	0.016
a_1	-0.0987	0.0632
a_2	0.2048	0.0877
a_3	0.52745	0.15986
a_4	-0.450223	0.166446
a_5	0.159674	0.078435
a_6	-0.028399	0.017124
a_7	0.002032	0.001416

notice that in this case we included LH and Boo sources down to a 5σ flux limit, to increase the statistics available in the first two flux density bins. From the comparison of the raw and final counts we see that the latter are systematically lower by a factor 7 – 14% in the range $S \sim 1 - 10$ mJy. This deficiency appears to be counterbalanced by a 10 – 20% excess at fluxes 0.2–0.6 mJy. This sort of compensation is consistent with being the result of source deblending, i.e. of the splitting of confused (brighter) sources into multiple fainter ones (see Sect. 5.3 and paper III for more details).

It is interesting to note that none of the previous counts’ determinations (neither at 150 MHz nor at higher frequency) show the pronounced ‘bump’ that we observe at 150 MHz sub-mJy fluxes. We have therefore decided to update the existing source counts best fits (shown in Figs. 5.7 and 5.8) with a new one that better matches the faint end of the 150 MHz counts derived from our final catalogues. The slope of the counts is modeled by a 7-th order polynomial function defined in the log-log space, according to Eq. 5.13 (see Sect. 5.5 for more details). To better constrain the bright end of the counts, where the LoTSS Deep Fields provide poor statistics, we have included the counts derived from the TGSS (Intema et al. 2017). The resulting coefficient values and their uncertainties are listed in Table 5.4; the fitted curve is shown in Fig. 5.9.

Qualitative comparison with models

The source counts derived from the LoTSS Deep Fields provide unprecedented observational constraints to the shape of the source counts at 150 MHz sub-mJy

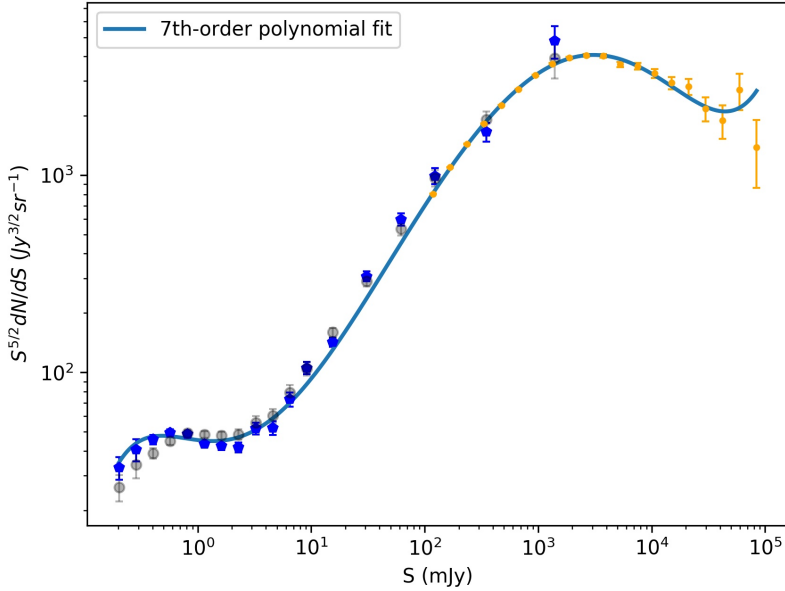


Figure 5.9: 150 MHz Euclidean normalized differential source counts as derived from the LoTSS Deep Fields: raw catalogue are indicated by transparent black circles and final catalogue by blue filled circles). Also shown are the counts obtained from the TGSS (Intema et al. 2017, orange filled circles), which better describe the counts’ bright end. Over-plotted is the best fit obtained by modeling the counts in the log-log space with a 7-th order polynomial function, according to Eq. 5.13 (see Table 5.4 for the values of the best-fit coefficients and associated errors).

fluxes. As such they can be compared with counts predictions based on existing evolutionary models of radio source populations. A comprehensive comparison with models is beyond the scope of this paper, and will be the subject of forthcoming papers, where counts and luminosity functions will be presented and discussed for various radio source populations. Here we only provide some first qualitative considerations.

In Figs. 5.7 and 5.8 we compare the LoTSS source counts to the 150 MHz determinations derived from the Wilman et al. (2008) and Bonaldi et al. (2019) simulated catalogues⁹ (black and dark violet shaded curves, respectively), as well as from Mancuso et al. (2017) models (light blue curve). We notice that the Bonaldi et al. (2019) and Wilman et al. (2008) source counts are very similar at the bright end and better reproduce the observations than Mancuso et al. (2017). On the other hand, Bonaldi et al. (2019) and Mancuso et al. (2017) counts are very similar at the faint end, and in better agreement with the observations than Wilman et al. (2008). Nevertheless, neither Bonaldi et al. (2019) nor Mancuso et al. (2017) can reproduce the pronounced bump at sub-mJy flux densities, observed in the counts derived from final catalogues (see Fig. 5.7, bottom panel, or Fig. 5.8). In addition all models appear to over-estimate the counts derived from our final catalogues at intermediate fluxes ($S \sim 2 - 20$ mJy).

In an attempt to better understand where the evolutionary models fail, we compare the observed source redshift distribution (using redshifts from paper IV) with those of the Bonaldi et al. (2019) simulated catalogue. We restrict this comparison to the EN1 field, as it is the deepest and has the most complete optical coverage among the three LoTSS Deep Fields.

In Fig. 5.10 we show the redshift distributions of the sources in the EN1 field (solid black lines) for various flux density bins. These distributions are compared with the simulated distributions based on Bonaldi et al. (2019) evolutionary models (blue histogram bars). We perform this analysis down to a flux limit of 0.25 mJy, i.e. down to a flux density where the effects of visibility function and incompleteness can be neglected. In the flux bins spanning from 0.25 to 0.75 mJy we see a clear deficiency of the simulated sources, in agreement with the observed excess in the counts. This deficiency is mainly associated with sources at $z < 1$. At larger fluxes ($S \geq 1$), on the other hand, we see an excess of simulated sources, which is also consistent with the deficiency observed in our counts in the range 2 – 20 mJy. This excess seems to be associated with either SFG or AGN at intermediate redshift ($1 < z < 2$).

⁹Bonaldi et al. (2019) present three simulated catalogues, each covering a different area of the sky. The one used here is the so-called *medium* tier, which covers a 25 deg² field of view, providing a very good match to the LoTSS Deep Fields. We use a new version of the catalogues originally presented in Bonaldi et al. (2019), which better reproduce the observations at the bottom and top of the covered frequency range (Bonaldi, private communication).

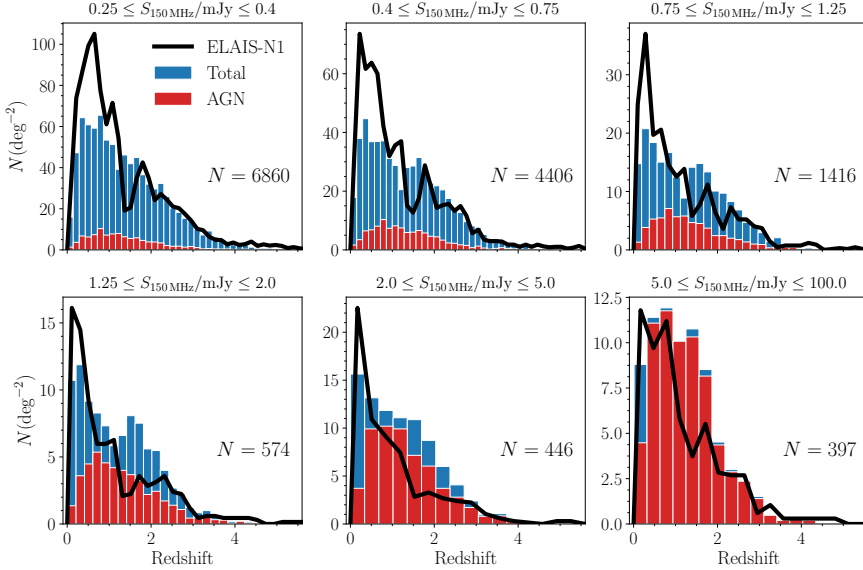


Figure 5.10: Redshift distribution of the simulated sources in [Bonaldi et al. \(2019\)](#) catalogue: the blue histogram corresponds to the total number of sources; the red histogram corresponds to the AGN component only. The solid black line shows the redshift distribution of the sources in the EN1 field. For a proper comparison the y-axis represents the source density in each catalogue. Each panel corresponds to a different flux density bin, increasing from left to right and from top to bottom.

5.7 Conclusions

In this paper, we have presented the source number counts derived from the LoTSS Deep Fields: the Lockman Hole (LH), the Boötes (Boo) and the Elais-N1 (EN1). With central rms noise levels of 22, 33, 17 $\mu\text{Jy beam}^{-1}$ the LH, Boo and EN1 fields are the deepest obtained so far at 150 MHz, allowing us to get unprecedented observational constraints to the shape of the source counts at 150 MHz sub-mJy fluxes. We compared the source counts derived from the LoTSS deep fields with other existing source-counts determinations from low-

and high- frequency radio surveys, and state-of-the-art evolutionary models. Our counts are in broad agreement with those from the literature, and show the well known upturn at \leq few mJy, which indicates the emergence of the star forming galaxy population. More interestingly, our counts show for the first time a very pronounced drop around $S \sim 2$ mJy, which results in a prominent ‘bump’ at sub-mJy fluxes. Such a pronounced ‘bump’ was not observed in previous counts’ determinations (neither at 150 MHz nor at higher frequency). We believe this is the result of a careful analysis aimed at deblending confused sources and removing spurious sources and artifacts from the radio source catalogues (see paper III). This ‘bump’ cannot be reproduced by any of the existing evolutionary models and appears to be associated with a low-redshift ($z < 1$) population of galaxies and/or AGN.

5.8 Acknowledgements

This paper is based (in part) on data obtained with the International LOFAR Telescope (ILT) under project code LC3_008. LOFAR (van Haarlem et al. 2013) is the Low Frequency Array designed and constructed by ASTRON. It has observing, data processing, and data storage facilities in several countries, that are owned by various parties (each with their own funding sources), and that are collectively operated by the ILT foundation under a joint scientific policy. The ILT resources have benefitted from the following recent major funding sources: CNRS-INSU, Observatoire de Paris and Université d’Orléans, France; BMBF, MIWF-NRW, MPG, Germany; Science Foundation Ireland (SFI), Department of Business, Enterprise and Innovation (DBEI), Ireland; NWO, The Netherlands; The Science and Technology Facilities Council, UK ; Istituto Nazionale di Astrofisica (INAF), Italy. This paper is based on the data obtained with the International LOFAR Telescope (ILT). The Leiden LOFAR team acknowledge support from the ERC Advanced Investigator programme NewClusters 321271 and the VIDI research programme with project number 639.042.729, which is financed by the Netherlands Organisation for Scientific Research (NWO). AD acknowledges support by the BMBF Verbundforschung under the grant 05A17STA. The Jülich LOFAR Long Term Archive and the German LOFAR network are both coordinated and operated by the Jülich Supercomputing Centre (JSC), and computing resources on the supercomputer JUWELS at JSC were provided by the Gauss Centre for supercomputing e.V. (grant CHTB00) through the John von Neumann Institute for Computing (NIC). TMS and DJS acknowledge the Research Training Group 1620 ‘Models of Gravity’, supported

by Deutsche Forschungsgemeinschaft (DFG) and support of the German Federal Ministry for Science and Research BMBF-Verbundforschungsprojekt D-LOFAR IV (grant number 05A17PBA). PNB is grateful for support from the UK STFC via grant ST/R000972/1. MJH acknowledges support from the UK Science and Technology Facilities Council (ST/R000905/1). IP and MB acknowledge support from INAF under PRIN SKA/CTA "FORECaST" and PRIN MAIN STREAM "SAuROS" projects, as well as from the Ministero degli Affari Esteri e della Cooperazione Internazionale - Direzione Generale per la Promozione del Sistema Paese Progetto di Grande Rilevanza ZA18GR02. JS is grateful for support from the UK STFC via grant ST/R000972/1. MJJ acknowledges support from the UK Science and Technology Facilities Council [ST/N000919/1] and the Oxford Hintze Centre for Astrophysical Surveys which is funded through generous support from the Hintze Family Charitable Foundation. RK acknowledges support from the Science and Technology Facilities Council (STFC) through an STFC studentship via grant ST/R504737/1. WLW acknowledges support from the ERC Advanced Investigator programme NewClusters 321271. WLW also acknowledges support from the CAS-NWO programme for radio astronomy with project number 629.001.024, which is financed by the Netherlands Organisation for Scientific Research (NWO). KLE acknowledges financial support from the Dutch Science Organization (NWO) through TOP grant 614.001.351. This research made use of APLpy, an open-source plotting package for Python hosted at <http://aplpy.github.com>.

5.A Appendix

Table 5.5: 150 MHz normalized differential radio-source counts as derived from the Lockman Hole field. S_{\min} and S_{\max} are the minimum and maximum flux densities (expressed in mJy), respectively. Δ denotes the flux density intervals. x is the geometric mean of S_{\min} and S_{\max} . N_S : Number of sources in respective bins. N is the normalized source counts and σ is the Poissonian errors on the normalized counts. Sys^+ and Sys^- are the systematic errors. N_c^{cor1} and N_c^{cor2} are the normalized counts with no systematic corrections applied and normalized counts with no systematic corrections and no visibility function applied, respectively. The tables for the Boötes and Elais-N1 fields are given in Table 5.6 and 5.7, respectively.

S_{\min}	S_{\max}	ΔS	x	N_S	$N_{-\sigma}^{+\sigma}$	Sys^-	Sys^+	N_c^{cor1}	N_c^{cor2}
0.23	0.32	0.09	0.27	5905	$39.51^{+0.48}_{-0.48}$	5.53	2.38	1.19	1.45
0.32	0.45	0.13	0.38	5463	$45.68^{+0.61}_{-0.61}$	2.18	2.74	1.02	1.12
0.45	0.64	0.19	0.54	4002	$50.25^{+0.80}_{-0.80}$	0.32	2.62	1.00	1.05
0.64	0.91	0.27	0.76	2447	$50.97^{+1.03}_{-1.03}$	0.04	2.26	1.01	1.03
0.91	1.29	0.38	1.08	1313	$44.16^{+1.25}_{-1.25}$	0.00	1.67	1.01	1.02
1.29	1.82	0.53	1.53	764	$43.01^{+1.61}_{-1.56}$	0.00	1.60	1.01	1.02
1.82	2.57	0.75	2.16	463	$43.31^{+2.11}_{-2.01}$	0.00	1.98	1.01	1.02
2.57	3.64	1.07	3.06	297	$46.50^{+2.86}_{-2.70}$	0.00	2.47	1.01	1.01
3.64	5.14	1.51	4.32	205	$54.06^{+4.04}_{-3.78}$	0.00	3.37	1.01	1.01
5.14	7.27	2.13	6.12	153	$67.62^{+5.91}_{-5.47}$	0.00	3.99	1.01	1.01
7.27	10.3	3.01	8.65	139	$103.2^{+9.5}_{-8.8}$	0.00	4.03	1.01	1.01
10.3	20.6	10.3	14.6	188	$150.0^{+11.7}_{-10.9}$	0.0	2.6	1.01	1.01
20.6	41.1	20.6	29.1	122	$275.3^{+27.2}_{-24.9}$	0.0	1.08	1.01	1.01
41.1	82.3	41.1	58.2	85	$541.5^{+65.1}_{-58.7}$	0.1	2.2	1.01	1.01
82.3	164	82.3	116.4	50	$900.5^{+145.4}_{-127.3}$	2.3	4.0	1.01	1.01
164	658	494	329	44	1776^{+308}_{-268}	2	11	1.00	1.00
658	2633	1975	1317	21	6791^{+1805}_{-1482}	24	91	1.01	1.01
2633	10530	7899	5266	1	2578^{+3929}_{-2139}	1	48	1.00	1.00

Table 5.6: Bootes 150 MHz source counts. See Table 5.5 for the caption

S_{\min}	S_{\max}	ΔS	x	N_S	$N_{+\sigma}$	S_{sys}^-	S_{sys}^+	$N_c^{\text{cor}1}$	$N_c^{\text{cor}2}$
0.33	0.47	0.13	0.39	3939	$44.57^{+0.70}_{-0.70}$	2.21	3.33	1.06	1.21
0.47	0.66	0.19	0.44	3251	$52.07^{+0.33}_{-0.33}$	0.40	3.42	1.01	1.08
0.55	0.93	0.27	0.78	2000	$51.25^{+1.17}_{-0.97}$	0.00	2.91	1.03	1.06
0.93	1.312	0.39	1.11	1088	$46.07^{+1.44}_{-1.44}$	0.04	2.20	1.02	1.04
1.32	1.87	0.55	1.59	651	$45.31^{+1.40}_{-1.88}$	0.00	2.47	1.02	1.02
1.87	2.64	0.77	2.22	373	$43.40^{+2.36}_{-2.25}$	0.00	2.91	1.02	1.02
2.64	3.73	1.09	3.14	263	$59.75^{+3.91}_{-3.69}$	0.00	4.43	1.01	1.18
3.73	5.27	1.54	4.43	152	$49.94^{+4.38}_{-4.05}$	0.00	4.30	1.01	1.02
5.27	7.46	2.18	6.27	147	$81.06^{+7.24}_{-6.69}$	0.00	6.78	1.01	1.02
7.46	10.55	3.09	8.87	126	$116.7^{+11.33}_{-10.4}$	0.00	6.50	1.01	1.01
10.55	21.09	10.55	14.91	140	$139.2^{+12.76}_{-11.77}$	0.00	3.29	1.01	1.01
21.09	42.18	21.09	29.83	100	$281^{+30.91}_{-28.10}$	0.0	1.30	1.02	1.01
42.18	84.36	42.18	59.65	73	$579.2^{+75.72}_{-67.79}$	0.58	2.83	1.01	1.01
84.36	168.7	84.36	119.3	45	$1010^{+173.1}_{-150.6}$	5.22	5.45	1.01	1.01
168.7	674.9	506.2	337.5	28	$1411^{+317.1}_{-298.7}$	3.57	11.34	1.01	1.01
674.9	2700	2025	1350	12	4798^{+1785}_{-1385}	9.21	47.8	1.00	1.00

Table 5.7: Elais-N1 150 MHz source counts. See Table 5.5 for the caption.

S_{\min}	S_{\max}	ΔS	x	N_S	$N_{-\sigma}^{+\sigma}$	Sys ⁻	Sys ⁺	N_c^{cor1}	N_c^{cor2}
0.17	0.24	0.07	0.20	6013	$36.13^{+0.43}_{-0.42}$	6.55	2.08	1.21	1.32
0.24	0.34	0.10	0.29	5399	$42.32^{+0.56}_{-0.55}$	2.48	2.33	1.03	1.08
0.34	0.48	0.14	0.40	3697	$45.04^{+0.74}_{-0.74}$	0.78	2.08	1.01	1.03
0.48	0.68	0.20	0.57	2257	$44.53^{+0.96}_{-0.94}$	0.10	1.76	1.00	1.01
0.68	0.96	0.28	0.81	1308	$43.04^{+1.22}_{-1.19}$	0.00	1.39	1.00	1.01
0.96	1.36	0.40	1.15	743	$40.88^{+1.55}_{-1.50}$	0.00	1.09	1.00	1.01
1.36	1.93	0.56	1.62	391	$36.04^{+1.92}_{-1.82}$	0.00	0.92	1.00	1.01
1.93	2.73	0.80	2.30	258	$39.93^{+2.64}_{-2.49}$	0.00	1.31	1.01	1.01
2.73	3.86	1.13	3.24	176	$45.78^{+3.71}_{-3.45}$	0.00	1.93	1.01	1.01
3.86	5.46	1.60	4.60	115	$50.28^{+5.12}_{-4.68}$	0.00	2.46	1.01	1.01
5.46	7.71	2.26	6.50	80	$58.72^{+7.30}_{-6.56}$	0.00	2.34	1.00	1.01
7.71	10.91	3.20	9.17	65	$80.12^{+11.17}_{-9.93}$	0.00	1.92	1.00	1.00
10.91	21.82	10.91	15.43	101	$134.5^{+14.72}_{-3.38}$	0.00	1.75	1.01	1.01
21.82	43.64	21.82	30.86	91	$340.7^{+39.46}_{-35.72}$	0.00	1.07	1.00	1.00
43.64	87.27	43.64	61.71	62	$657.2^{+94.06}_{-83.46}$	0.32	2.23	1.00	1.00
87.27	174.5	87.27	123.4	36	$1080^{+209.9}_{-179.9}$	2.55	4.10	1.00	1.00
174.5	698.2	523.6	349.1	18	$1214^{+353.7}_{-286.2}$	2.05	7.54	1.01	1.01
698.2	2793	2095.0	1396.0	5	$2689^{+1741.0}_{-1203}$	6.47	30.68	1.00	1.00

